INTERFACE

rsif.royalsocietypublishing.org

Research

Cite this article: Antoine EE, Cornat FP, Barakat AI. 2016 The stentable *in vitro* artery: an instrumented platform for endovascular device development and optimization. *J. R. Soc. Interface* **13**: 20160834. http://dx.doi.org/10.1098/rsif.2016.0834

Received: 17 October 2016
Accepted: 28 November 2016

Subject Category:
Life Sciences – Engineering interface

Subject Areas:
biomaterials, biomedical engineering, biomechanics

Keywords:
in vitro artery, stent, shear stress, collagen I hydrogel, real-time quantitative cellular imaging, endothelial wound healing

Author for correspondence:
Abdul I. Barakat
e-mail: barakat@ladhyx.polytechnique.fr

Electronic supplementary material is available online at https://dx.doi.org/10.6084/m9.figshare.c.3634253.

THE ROYAL SOCIETY PUBLISHING

The stentable *in vitro* artery: an instrumented platform for endovascular device development and optimization

Elizabeth E. Antoine, François P. Cornat and Abdul I. Barakat

Hydrodynamics Laboratory (LadHyX), Ecole Polytechnique, Route de Saclay, 91128 Palaiseau, France

EEA, 0000-0001-8116-9585; AIB, 0000-0002-7551-3631

Although vascular disease is a leading cause of mortality, *in vitro* tools for controlled, quantitative studies of vascular biological processes in an environment that reflects physiological complexity remain limited. We developed a novel *in vitro* artery that exhibits a number of unique features distinguishing it from tissue-engineered or organ-on-a-chip constructs, most notably that it allows deployment of endovascular devices including stents, quantitative real-time tracking of cellular responses and detailed measurement of flow velocity and lumenal shear stress using particle image velocimetry. The wall of the stentable *in vitro* artery consists of an annular collagen hydrogel containing smooth muscle cells (SMCs) and whose lumenal surface is lined with a monolayer of endothelial cells (ECs). The system has *in vivo* dimensions and physiological flow conditions and allows automated high-resolution live imaging of both SMCs and ECs. To demonstrate proof-of-concept, we imaged and quantified EC wound healing, SMC motility and altered shear stresses on the endothelium after deployment of a coronary stent. The stentable *in vitro* artery provides a unique platform suited for a broad array of research applications. Wide-scale adoption of this system promises to enhance our understanding of important biological events affecting endovascular device performance and to reduce dependence on animal studies.

1. Introduction

Although *in vivo* studies are the gold standard for understanding disease processes and screening new treatments, their complexity, often limited predictive capacity, prohibitive cost and ethical concerns demand alternative, novel approaches. In the specific case of vascular disease, there is a critical need for systems that enable controlled, quantitative assessment of the efficacy of new drugs as well as optimization of implantable devices [1,2]. For instance, although endovascular stents have become the primary treatment for atherosclerotic and thrombotic disease in both coronary and peripheral blood vessels [3], catastrophic complications such as late stent thrombosis (LST) and in-stent restenosis (ISR) still pose significant risk to patients [3]. Therefore, there is a clear clinical need for novel stent concepts; however, assessment of the efficacy of such concepts and optimization of their performance is both difficult and expensive using only *in vivo* data.

In vitro studies using two-dimensional cell culture systems have been invaluable for elucidating the complex biological mechanisms that lead to events such as LST and ISR and have provided significant insight into the extent of communication among different cell types found in the arterial wall as well as coupling between the mechanical stress field and biological endpoints. Such studies have demonstrated, for example, that altered fluid shear stress, such as that found around struts of implanted stents, perturbs the function of the endothelial monolayer lining the arterial wall [4]. Smooth muscle cells (SMCs) have been shown to change phenotype in response to loss of integrity of an adjacent endothelium, as occurs during stent deployment [5], while simultaneously regulating endothelial cell (EC) function [6]. While *in vitro* studies have contributed greatly to

our understanding of specific biological mechanisms of post-stent complications, translation of results obtained under such idealized conditions to clinical applications remains a challenge. Experiments performed on two-dimensional substrates do not provide the three-dimensional micro-environment that has been repeatedly shown to play a vital role in regulating essential functional endpoints including cell morphology, signalling and migration [7,8]. Indeed, hydrogel-based three-dimensional engineered tissues have been shown to better mimic *in vivo* functionality than two-dimensional cultures [9,10].

Recently, more complex experimental *in vitro* platforms have been developed in order to address these limitations. Implantable tissue-engineered blood vessels (TEBV) are being designed for use in regenerative medicine. Modern TEBV systems are capable of mimicking physiological response and functionality to a high degree [11,12]. For example, a recently developed TEBV composed of collagen hydrogel, fibroblasts or stem cells, and ECs exhibits contractility, vasoactivity and inflammatory response [13]. A major limitation of such tissue-mimicking TEBV systems is their lack of compatibility with real-time imaging, which inhibits quantification and assessment of dynamic cellular processes.

In parallel, there is considerable ongoing work in the development of *in vitro* diagnostic tools for the study of biological phenomena. These 'lab-on-a-chip' or 'organ-on-a-chip' devices are designed for high-resolution cellular imaging and/or quantitative assays. These systems vary in complexity; one recent example is a multi-layered gelatin-based microchannel incorporating fibroblasts, SMCs, and a complete endothelium, all of which remain viable for at least 3 days [14]. However, this and similar micro-scale diagnostic platforms are not adapted for investigation of macro-scale vasculature or endovascular device implantation [14–16].

Here we present a novel platform, dubbed the 'stentable *in vitro* artery', which addresses many of the limitations of *in vivo* and previous *in vitro* work. Specifically, the proposed system combines physiological dimensions, flow and cellular components with advanced high-resolution imaging and quantification of cellular behaviour. Moreover, the stentable *in vitro* artery allows deployment of endovascular devices used clinically, including balloons and stents, and the measurement of the effect of these devices on the flow field and wall shear stress (WSS). Beyond its usefulness for endovascular device research, the system constitutes a versatile platform for a variety of vascular research applications.

2. Material and methods

2.1. Cell culture

Bovine aortic ECs (gift of C. Boulanger, Georges Pompidou Hospital, Paris, France) and bovine aortic SMCs (Tebu-Bio) were used in this study. ECs were cultured in Dulbecco's modified Eagle's medium (DMEM; Invitrogen) supplemented with 10% fetal bovine serum (Invitrogen) and 1% penicillin/streptomycin (Invitrogen), while SMCs were cultured in bovine SMC growth medium (Tebu-Bio). Cell cultures were maintained in a 5% CO_2 atmosphere at 37°C in an incubator; ECs in passage 7 and SMCs in passage 6 were used. Immediately prior to each experiment, SMCs were labelled with red fluorescent Vybrant CM-DiI (Life Technologies) while ECs were labelled with green fluorescent Vybrant DiO (Life Technologies) for time-lapse imaging.

2.2. Smooth muscle cell-embedded collagen hydrogel

Collagen I was obtained from rat tail tendon as described previously [17]. Briefly, tendons were extracted from rat tails, dissolved in a solution of 0.01 mol l^{-1} hydrochloric acid (HCl; Sigma), and centrifuged at 30 000*g* and 4°C for 1 h. The supernatant was cooled to −80°C, lyophilized, and stored at −20°C for up to six months. In preparation for each experiment, the lyophilized collagen was reconstituted to 12 mg ml^{-1} in 0.01 mol l^{-1} HCl and stored at 4°C for no more than one week. Collagen hydrogels mimicking the arterial wall were fabricated by combining 1 ml cold acidic collagen solution with 1 ml cold neutralizing buffer containing 200 µl 10× concentrated DMEM (Sigma), 756 µl EC culture medium, 43.5 µl of 1 mol l^{-1} sodium hydroxide (Sigma) and 400 000 SMCs for a final pH of 8.4, collagen concentration of 6.0 mg ml^{-1}, and SMC concentration of 200 000 cells ml^{-1} [17].

2.3. Device design and assembly

The stentable *in vitro* artery is represented schematically in figure 1*a* and by a photograph in figure 1*b*. Following Buchanan *et al*. [18], fluorinated ethylene propylene (FEP) tubing (inner diameter 4.8 mm, wall thickness 0.8 mm, length 60 mm) (Fisher) was plasma-treated to activate surface hydroxyl groups and cross-linked with 1% polyethylenimine (Sigma) for 10 min followed by 0.1% glutaraldehyde (Sigma) for 20 min to render the surface hydrophilic. After treatment, the FEP was thoroughly dried by aspiration, inserted through holes longitudinally drilled in a 24 mm wide × 60 mm long × 10 mm high acrylic frame, and fitted at the ends with custom-machined stainless steel sleeves with concentric 3.0 mm ports. The neutralized collagen/SMC solution was carefully stirred with a spatula, pipetted into the prepared device, fitted with a 3.0 mm stainless steel pin and allowed to polymerize at 37°C for 20 min, resulting in a hydrogel with a compression modulus of 4600 ± 1500 Pa and average pore diameter of 1.4 ± 0.1 µm (mean ± s.e.m.) [17]. After polymerization, the pin was removed from the device, leaving a 3.0 mm channel centred in the hydrogel. Finally, the channel was seeded in multiple stages over a period of 1 h, rotating the device between each stage, with a 1.8 million cells ml^{-1} suspension of ECs to form a monolayer covering the channel lumen. The *in vitro* artery was encased in a transparent frame for live fluorescence imaging and quantification of biological response to a range of mechanical and/or biochemical stimuli.

In preparation for imaging, a 24 × 60 mm glass coverslip was glued to the bottom of the acrylic frame using vacuum grease. The device was filled with phosphate buffered saline (PBS) and sealed with a matching acrylic coverslip on the top of the frame to prevent evaporation of the PBS bath during the experiment. Because the refractive index of FEP closely matches those of PBS and cell-culture medium, this configuration permits acquisition of undistorted transmitted light and fluorescence images on an epifluorescence microscope.

2.4. Perfusion

After assembly, the *in vitro* artery was submitted to preconditioning flow using EC culture medium supplemented with 25 mM HEPES (Gibco). First, the *in vitro* artery was placed in an incubator (37°C, 5% CO_2) and connected via luer adapters and silicone tubing to a syringe pump (Harvard Apparatus) outside the incubator. An initial flow rate of 0.016 ml min^{-1}, corresponding to a WSS less than 0.1 mPa (0.001 dyn cm^{-2}), was applied in order to provide media replacement with minimal shear during endothelial adhesion and spreading. Over a period of 72 h, the flow rate was increased over three orders of magnitude in a stepwise fashion to ultimately achieve coronary flow without damaging the newly formed endothelium. During flow preconditioning,

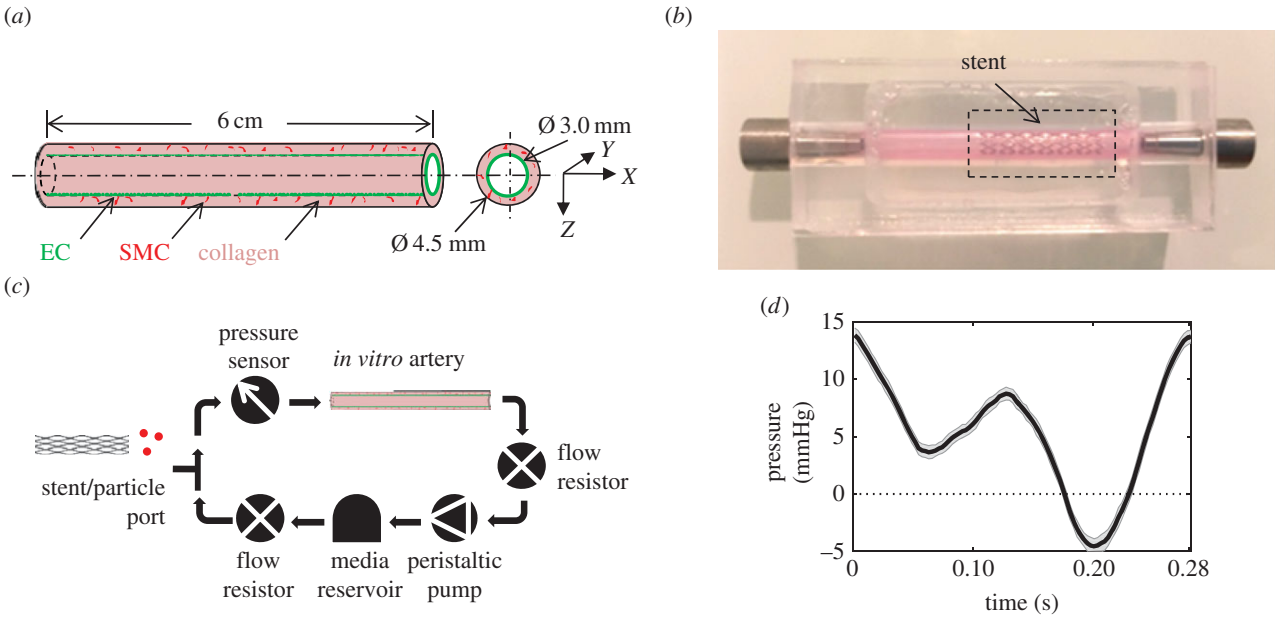

Figure 1. The stentable *in vitro* artery. (*a*) The artery is composed of an annular collagen I hydrogel containing 200 000 ml^{-1} smooth muscle cells (SMCs) lined with a monolayer of endothelial cells (ECs). The dimensions are typical of the human coronary artery. (*b*) The hydrogel is injected into a polymer tube through stainless steel adapters which are subsequently connected to the pulsatile flow loop. The artery (here with an embedded coronary stent) is submerged in a PBS bath for imaging. (*c*) A pulsatile flow profile is generated by adjustment of flow rate, peristaltic tubing diameter and position of flow resistance valves and is measured using a pressure sensor. A three-way valve enables stent deployment and injection of tracer particles into the circulating medium. (*d*) The ultimate flow condition has a mean Reynolds number of 360 and Womersley number of 16, matching human coronary flow. The pressure plotted is mean $\pm$ s.d.

the *in vitro* artery was removed from the incubator, transferred from the syringe pump to the pulsatile flow loop in figure 1*c* and mounted on an epifluorescence microscope for imaging. Pulsatile flow loop components included a peristaltic flow pump (Masterflex), peristaltic tubing (Masterflex L/S 16), media reservoir, flow resistance valves (Flow-Rite), and a pressure sensor (PendoTech) and were connected using luer adapters and silicone tubing. A temperature of 31 $\pm$ 0.5°C was maintained in the *in vitro* artery by placing the media reservoir in a circulating water bath at 38°C.

The final flow rate applied to the *in vitro* artery was designed for hydrodynamic similarity with the flow of blood in the human coronary artery. A time-averaged Reynolds number of 360 and a Womersley number of 16 with a pressure amplitude of 20 mmHg (2.7 kPa) (figure 1*d*) were achieved at a mean flow rate of 40 ml min^{-1} and by adjusting the position of the flow resistors. Non-dimensional parameters were calculated based on the nominal channel diameter (3.0 mm), nominal pump roller frequency (3.5 Hz), and density and dynamic viscosity of culture medium at 37°C (1000 kg m^{-3} [19] and 0.78 mPa s [18], respectively). At this flow rate, the mean shear stress on the endothelium is estimated, based on an assumption of Poiseuille flow, to be 0.2 Pa (2 dyn cm^{-2}). The system was subjected to this flow condition for 18 h before stent deployment.

2.5. Stent deployment

After flow preconditioning, an 18 mm long bare metal stainless steel stent with 80 µm thick struts (Tsunami Gold, Terumo) was deployed in the *in vitro* artery. First, the balloon catheter on which the stent was mounted was connected to an inflation syringe (Merit Medical), filled with PBS, purged of air and connected to a three-way valve in the flow loop. Flow in the *in vitro* artery was paused. The catheter was inserted through the three-way valve to the centre of the *in vitro* artery and inflated to a pressure of 12 atm (1.2 MPa), overexpanding the stent to a diameter of 3.1 mm. This overexpansion was targeted in order to ensure retention within the artery during and after removal of the balloon. After deflation, the catheter was withdrawn and flow was restarted. This process can be visualized in electronic supplementary material, video S1.

2.6. Time-lapse imaging

Cell migration was recorded using time-lapse imaging on an epifluorescence microscope with a motorized stage (Ti-E, Nikon), 1280 × 1024 CCD camera (Retiga 1300C, Qimaging) and 4× magnification (1.66 µm pix^{-1}). Images were acquired at 1 frame per hour prior to stent deployment and at 2 frames per hour after stenting. A halogen lamp was used for phase-contrast illumination while a mercury lamp was used for fluorescence illumination, with a FITC filter for imaging ECs and a TRITC filter for imaging SMCs. At each time point, phase-contrast and fluorescence images were acquired at each position of an 18 × 4 grid with 5% overlap in x–y covering the entire *in vitro* artery. Each image sequence was acquired with the focal plane either in the centre of the channel or at a plane tangent to the lumen. Image acquisition was controlled through µManager, an ImageJ plugin [20]. Preliminary image processing, stitching and minor rotation to align the channel with the imaging axis were performed in FIJI, an ImageJ suite [21].

2.7. Quantification of endothelial wound healing

All endothelial wound healing analysis was performed in Matlab. First, two regions of interest (ROIs) of similar size were selected from the FITC (endothelial) channel, each containing a well-defined section of wound: one ROI upstream of the stent and one ROI within the stent. Whole-image shifts in the time-lapse sequence were corrected using a particle image velocimetry (PIV)-based image registration scheme. Because the wound boundary is poorly defined due to variation in individual cell position as well as heterogeneous cell fluorescence, bulk analysis was performed on profiles obtained by averaging the fluorescence along the length of the wound. Subsequently, each profile was normalized to reduce the influence of lighting variations. The speed of wound healing was computed

robustly using parametric variation of the intensity threshold used to estimate boundary position as well as the number of frames (time points) used in linear regression for slope estimation. The normalized threshold was varied between 0.1 and 0.5 in steps of 0.05, while the number of frames used for regression was between 16 and 21 (7.5–10 h post-stenting). This parametric variation provided 54 'replicates' for each wound boundary (top and bottom) within each ROI (upstream and in-stent). Comparisons were performed using ANOVA and Tukey's *post hoc* test. Intermediate steps of wound healing analysis can be found in electronic supplementary material, figure S1.

2.8. Tracking smooth muscle cells

TRITC (smooth muscle) fluorescence image series were first registered using a similar method to that described above to correct for whole-image shifts. SMC tracking was performed in two ROIs in a 400 µm wide section of collagen hydrogel at the channel wall: one ROI upstream of the stent and one ROI adjacent to stent. In FIJI, images were binarized using a user-defined threshold (constant for all datasets) and preprocessed using an erosion/dilation sequence to regularize cells for tracking. Tracking was performed using the MTrack2 plugin, with a minimum radius of 5 µm for an object to be considered a cell and a maximum allowable speed of 50 µm h^{-1} for accurate cell matching between frames. A custom Matlab script was used to load the results generated by FIJI/MTrack2, compute cell velocity and persistence and perform statistical analysis. Only cells present in at least three sequential frames were considered for analysis. Cell velocity was broken into three different metrics: net velocity U parallel to the channel wall (positive U = migration in the direction of flow), net velocity V perpendicular to the channel wall (positive V = migration towards the wall) and speed, which is calculated as the total cell path length divided by total time and is, therefore, larger in magnitude than either U or V.

2.9. Particle image velocimetry

The PBS seeded with 3.2 µm red fluorescent polymer microspheres (Thermo Scientific) was perfused in the *in vitro* artery under the same flow conditions as previously (time-averaged Reynolds number 360, Womersley number 16, pressure amplitude 20 mmHg (2.7 kPa)). Micro-PIV [22] was performed on the same microscope used for time-lapse imaging, with a 4× 0.2 NA objective and TRITC filter. For these imaging parameters, the depth of correlation of PIV measurements [23] was estimated to be 85 µm. Particle images were acquired using a double-frame CCD camera (LaVision) with magnification of 1.85 µm pix^{-1}, laser illumination via a double-pulsed Nd:YAG laser frequency-doubled to 532 nm (Litron), and DaVis software for synchronization of laser and camera. One thousand particle image pairs were acquired at each of 11 overlapping positions along the channel wall, at a frequency of 10 Hz with 100 µs inter-frame time. Images were preprocessed using mean background subtraction to increase signal-to-noise ratio, reduce effects of uneven illumination and remove reflections from stent struts.

All PIV analysis was performed using PRANA, a Matlab-based open-source PIV suite. Owing to the complexity of the experiment, several steps were necessary to recover a time-resolved, accurate velocity field coherent across all imaging positions. Because the maximum laser pulse and frame rate (10 Hz) resulted in undersampling and data acquisition was not synchronized with the pump, initial PIV analysis was performed to improve the time resolution of final velocity fields using a method similar to that described by Poelma *et al.* [24]. Assuming reproducibility of the flow field from one pulse to the next, this was achieved by the following: first, image pairs were correlated using large windows, adaptive windowing [25] and single-pass robust phase correlation [26], next the mean velocity at the channel centreline was computed for each image pair, then the periodicity of flow (0.286 s) was computed from the maximum peak of the discrete Fourier transform of the mean velocity signal, and finally, phase-unwrapping was performed on the sequence of image pairs to order them within a single flow period. Because the resulting temporal resolution was higher than strictly necessary for this analysis, the effective resolution was reduced to 167 frames per period by grouping unwrapped images into bins containing six pairs each. All further PIV analysis was performed using sum-of-correlation within each group [27]. This had the effect of increasing the signal-to-noise ratio and, therefore, the accuracy of PIV measurements at each of the remaining time points.

Using the unwrapped, binned image pairs, a second run of PIV was performed to identify regions of each image where particles could not be visualized. In this experiment, this was critical due to the presence of the stent which blocked imaging in a significant portion of the channel. In this run, high-resolution two-pass PIV with small windows was performed using universal outlier detection (UOD) [28] and thresholding to flag vectors inconsistent with surrounding measurements. Vectors that were flagged in 50% or more of all image pairs in sequence were determined to be unreliable, and the corresponding positions were combined to form a mask which was applied to all future analysis steps. This mask was further modified to include masking of the region outside the channel wall.

A final PIV run was performed using the combined validation/wall mask, 64 × 128 pixel correlation regions with 75% overlap windowed to 32 × 64 pixels with a Gaussian filter, two-pass robust phase sum-of-correlation, three-point Gaussian peak fitting and UOD validation to obtain velocity fields with a vector resolution of 14.8 µm × 29.6 µm × 3 ms in X, Y and T, respectively. Each vector field was shifted to move peak flow to the initial time point, enabling the measurements for each imaging position to finally be stitched into a single, coherent vector field covering a 16.65 × 1.85 mm section of the channel.

2.10. Wall shear stress measurement

Five ROIs along the channel wall were selected for WSS measurement. Four ROIs beginning 25 µm downstream of stent struts and extending an additional 280 µm downstream were analysed. All regions were 550 µm high and vertically centred over the channel wall. For comparison, WSS was also measured in a control ROI with the same dimensions. The boundary layer development length for (steady) laminar flow is $L = 0.05 \times Re \times D$; for a Reynolds number Re of 360 and strut thickness D of 80 µm, this length is 1.4 mm. Therefore, the downstream ROI was placed 2 mm downstream of the stent in order to provide measurements representative of the undisturbed flow field.

In order to identify the channel wall position, the brightfield image was sharpened using the Matlab function *graydiffweight*, filtered and binarized. The profile of the wall was smoothed using a median filter, and subpixel wall positions were identified by fitting with a cubic spline function [29]. In order to calculate the WSS for each ROI, vector fields were first filtered using proper orthogonal decomposition with 95% energy recovery. Subsequently, thin plate spline radial basis functions were computed for a 5 × 5 vector grid at each wall position (9–10 positions per stent ROI, 63 positions for the downstream ROI) and used to obtain an enhanced estimation of the velocity gradient tangential to the wall at each time during the cycle (167 time points) [30]. The time-varying WSS was finally averaged for all wall positions within each ROI. Comparisons between time-averaged WSS for each ROI were performed using ANOVA and Tukey's *post hoc* test.

2.11. Computational flow model

The experimentally measured flow and WSS were compared with a computational fluid dynamics (CFD) model of the

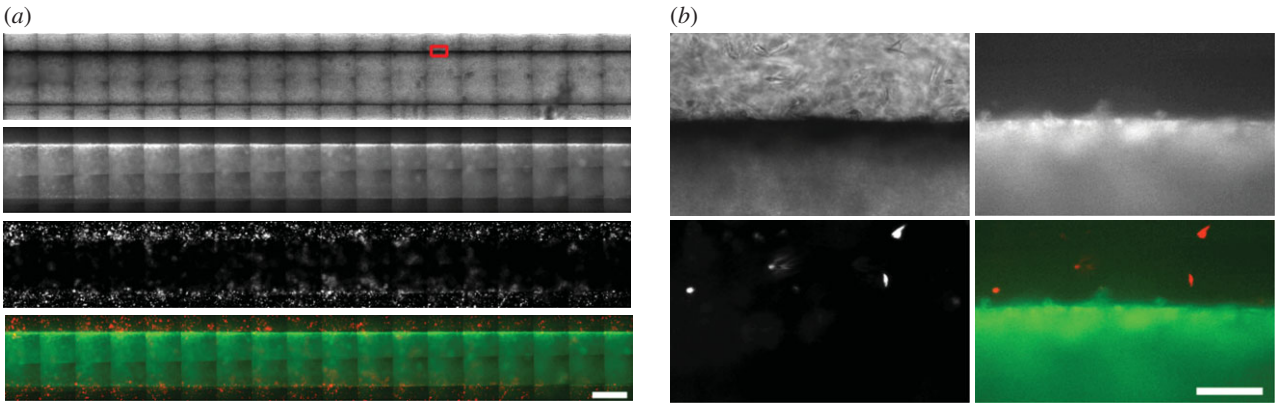

Figure 2. Cell organization in the stentable *in vitro* artery. (*a*) After 72 h of flow preconditioning, the artery contains a stable endothelial cell monolayer and elongated smooth muscle cells and is ready for stent insertion. From top to bottom: phase-contrast, endothelium, smooth muscle, overlay of endothelium (green) and smooth muscle (red). Scale bar, 2 mm. Flow is from left to right. Images were acquired at the central plane of the channel in order to visualize cell distribution at the lumen. The repeating grid pattern is an artefact of uneven sample illumination. (*b*) Magnification of the region indicated by the red box on the phase-contrast image in panel (*a*). Scale bar, 200 µm.

in vitro artery in order to assess the validity of the values obtained. The CFD simulations were performed using the commercial finite-element multi-physics code COMSOL (v. 5.2a). The model geometry consists of a 3 mm diameter straight cylinder, representing the fluid within the *in vitro* artery, with cutouts corresponding to the struts of the deployed stent. The strut geometry for the simulations was simplified as a repeating diamond structure, including connecting struts while neglecting the rotation between diamond elements. Only a 7.5 mm long section of the stent was modelled in order to reduce computational time. Entrance and exit sections of 1.5 mm and 2.5 mm, respectively, were added in order to ensure developed flow within the stent. Struts were assumed to be embedded within the arterial wall to 50% of their height; therefore, the strut height in the model geometry was set to 40 µm. A further reduction in computational time was achieved by simulating only a 1/6 radial section of the fluid. The fluid geometry was meshed using a combination of prism and tetrahedral elements, with a total of 883 000 elements in the model. The time-averaged WSS over the entire lumenal surface was calculated using the described mesh and compared with the results using a mesh containing 10 times more elements; this difference was only 3%, confirming mesh independence. The model geometry and a representative section of the mesh are shown in figure 6*a*.

For the numerical model, the fluid was assumed to be Newtonian with the density and dynamic viscosity of culture medium reported above (1000 kg m^{-3} and 0.78 mPa s, respectively). A pulsatile flow with parabolic profile was imposed at the inlet, using the centreline velocity profile obtained from PIV measurements (figure 5*d*), while a zero-pressure condition was imposed at the outlet. A no-slip condition was imposed on the lumenal surface containing stent struts, while symmetry boundary conditions were imposed on the lateral walls. The spatial distribution of the flow field was computed implicitly using the generalized minimal residual nonlinear finite-element solver, and the temporal evolution was computed implicitly using a time-dependent solver with a temporal resolution of 5 µs. Simulations were performed over five pulsatile cycles and results were taken from the last, in order to ensure a time-periodic solution.

Because the stent geometry in the numerical model was idealized, it was not possible to evaluate WSS at the same ROIs as in the experimental measurements. Therefore, WSS from the numerical simulation was measured at four manually selected ROIs (I–IV) of the same length as those in the experimental measurements, located at various positions relative to stent struts, in addition to a downstream ROI placed identically to that of the experimental analysis. ROI positioning is indicated in figure 6*a*.

2.12. Supplementary immunostaining and live/dead imaging

In order to visualize cellular actin networks as well as cell survival after stent implantation, two additional *in vitro* arteries were constructed and preconditioned up to the point at which they would normally be transferred from the incubator to the pulsatile flow loop and mounted on the epifluorescent microscope for imaging. At this time, the first *in vitro* artery (for immunofluorescence, IF) was fixed with 4% paraformaldehyde (Alfa Aesar), permeabilized with 0.1% Triton X-100 (Sigma) in Tris-buffered saline (TBS; Sigma), incubated with a blocking buffer containing 5% bovine serum albumin (Sigma) and 0.01% Triton X-100 in TBS, stained with 1 : 100 Alexa Fluor 594 phalloidin (Life Technologies) for visualization of actin filaments and 1 : 1000 DAPI (Sigma) for visualization of cell nuclei, and rinsed thoroughly with blocking buffer before imaging.

The live/dead *in vitro* artery was implanted with a 14 mm long bare metal stent (Qualimed) overexpanded to 3.1 mm according to the same protocol as described in the section 'Stent deployment'. Immediately after stent deployment, the *in vitro* artery was flushed with PBS, incubated with 8 µM calcein AM (Life Technologies) (to stain live cells) and 8 µM ethidium homodimer-1 (Life Technologies) (to stain dead cells) in EC culture medium, and rinsed thoroughly with PBS before imaging.

For both the IF and the live/dead *in vitro* arteries, fluorescence images were acquired on the epifluorescence microscope described previously using a Hamamatsu Orca Flash-4.0 camera and 4×, 10× or 20× magnification.

3. Results

The *in vitro* artery incorporates a dense collagen hydrogel embedded with aortic SMCs, a 3 mm diameter central channel lined with aortic ECs, and perfusion by cell culture medium with a physiologically relevant pulsatile waveform (figure 1). The dimensions and dimensionless flow parameters (Reynolds and Womersley numbers) mimic those found in coronary arteries *in vivo*. After 3 days of initially steady and ultimately pulsatile flow preconditioning, the endothelium forms a continuous monolayer and the SMCs elongate along collagen fibres within the hydrogel. This can be seen in images of labelled live cells (figure 2) as well as fixed samples stained for cell nuclei and actin (electronic supplementary material, figure S2, video S2).

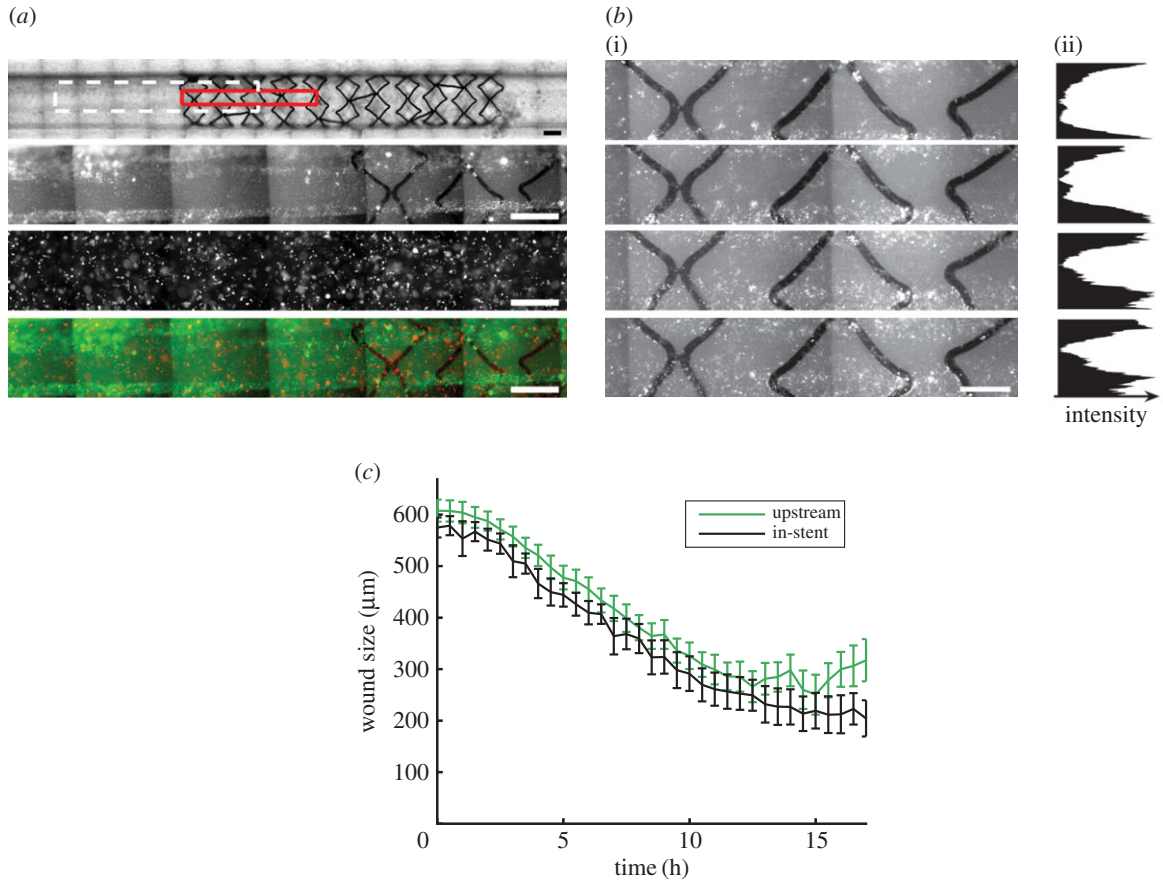

Figure 3. Endothelial wound healing in the stentable *in vitro* artery. (*a*) Stent deployment wounds the endothelium upstream of and within the stent. From top to bottom: phase-contrast, endothelium, smooth muscle, overlay of endothelium (green) and smooth muscle (red). The three lower frames show the region indicated by the white dashed box in the top image. Scale bar, 1 mm for all frames. Flow is from left to right. Images were acquired at a plane tangent to the channel lumen for time-lapse imaging for endothelial migration. (*b*) (i) Endothelial cells migrate to fill the wound in the region of interest highlighted by the red box on the phase-contrast image in panel (*a*). Frames shown are (top to bottom): 0, 5, 10 and 15 h post-stent. (ii) The mean intensity profile for each frame is used to estimate the rate of endothelial wound healing. Scale bar, 500 μm. (*c*) Wound size, calculated as the distance between the top and bottom wound front positions, has a similar magnitude and temporal profile for the regions upstream of and within the stent.

As occurs *in vivo* [31], insertion of the balloon catheter and deployment of the stent in the *in vitro* artery resulted in significant damage to the endothelial monolayer; specifically, a 600 μm wide swath of endothelium both upstream of and within the stent was completely sheared away (figure 3*a*). The vast majority of both SMCs and ECs in the *in vitro* artery remained viable (electronic supplementary material, figure S3). In the following sections, we describe endothelial wound healing, SMC motion and fluid dynamic shear stress alterations after deployment of the coronary stent.

3.1. Endothelial wound healing post-stenting

Following stent deployment, ECs migrated to fill damaged regions, including the large wound created by the stent and balloon catheter (figure 3*b*; electronic supplementary material, video S3). We quantified this wound healing by tracking the position of the endothelial front both upstream of and within the stent, using a robust algorithm implemented in Matlab (figure 3*c*). The endothelial front advanced at a nearly constant rate for the first 10 h post-stent, after which healing slowed to the end of the experiment. The overall rate of endothelial wound healing, defined as the average speed of endothelial front migration during the first 7.5–10 h post-stenting (detailed in the electronic supplementary material), was measured to be $15.4 \pm 0.8\ \mu m\ h^{-1}$. The two opposing wound fronts healed at different apparent rates ($13.7 \pm 0.5\ \mu m\ h^{-1}$ for the top wound front versus $17.1 \pm 1.0\ \mu m\ h^{-1}$ for the bottom wound front, $p < 0.0001$), a difference that is consistent with the positions of the fronts on the channel lumen relative to the imaging plane: the wound front with lower apparent velocity (top) is farther from the in-focus plane of the *in vitro* artery than the faster wound front (bottom) and, therefore, has a significant out-of-plane component that is not quantifiable in two-dimensional images. More importantly, the presence of the stent had no impact on the rate of endothelial wound healing ($15.5 \pm 0.4\ \mu m\ h^{-1}$ within the stent versus $15.3 \pm 0.4\ \mu m\ h^{-1}$ upstream of the stent, $p = 0.9927$).

3.2. Smooth muscle mobility within the collagen gel

In addition to endothelial wound healing, migration of SMCs (figure 4*a*; electronic supplementary material, video S4) can be visualized and quantified in the *in vitro* artery. We examined SMC migration in the hydrogel in regions both upstream of and immediately adjacent to the stent. Qualitatively, SMCs could be classified as either migratory or stationary, with migratory cells elongating and following short, random paths within the hydrogel (figure 4*a*). No apparent preferential migration towards the stent was identified. Quantitative analysis produces results in agreement with the qualitative observations (figure 4*b*). With 191 cells tracked in the upstream region and 428 tracked in the stent-adjacent region, both populations followed near-normal distributions of net velocity in

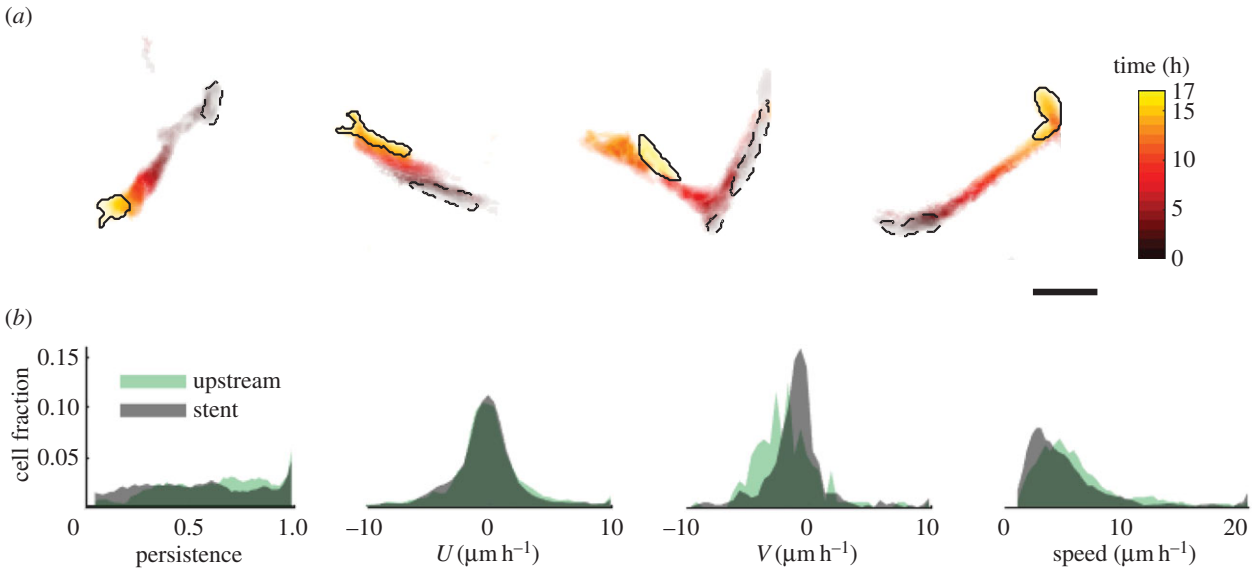

Figure 4. Smooth muscle cell (SMC) migration in the stentable *in vitro* artery. (*a*) SMCs are motile within the hydrogel, with widely varying trajectories, as shown by an overlay of images throughout the experiment for four example cells. Time is indicated in colour, and each cell is outlined at the first and last time points using dashed and solid lines, respectively. Scale bar, 50 μm. (*b*) SMC migration statistics, including persistence, velocity components *U* and *V*, and speed, are averaged over a 17 h period immediately following stent deployment and compared for cells in the collagen hydrogel upstream of the stent and adjacent to the stent.

both the *x*- and *y*-directions (*U* and *V*, respectively), with means near zero. Cell speed followed a skewed distribution reminiscent of a log-normal and was also similar in both regions albeit slightly increased upstream of the stent, with mean ± s.e.m. (median) speeds of 6.2 ± 0.3 (5.3) μm h^{-1} upstream of the stent and 5.3 ± 0.2 (4.3) μm h^{-1} adjacent to the stent as well as a small minority of cells moving at speeds up to 20 μm h^{-1} in both regions. Cell persistence, defined as the ratio of the net displacement to total path travelled by each cell, followed a nearly random distribution for both regions, consistent with the qualitative observation that SMC migration in the isotropic hydrogel was random and not directed.

3.3. Alterations in wall shear stress downstream of stent struts

Because ECs are highly sensitive to shear stress and flow perturbation, and as stent struts can induce significant perturbation of the flow field in the vicinity of the stent, high-resolution near-wall flow measurement is an important factor in understanding endothelial response to stenting [32]. By combining the *in vitro* artery with a synchronized camera and a pulsed laser, we were able to quantify flow alteration by the deployed stent in a large region of the artery including a significant portion of the stent as well as a downstream section (figure 5*a*). High-resolution velocity fields (figure 5*b*) were obtained using PIV, an optical technique for quantitative flow measurement well-adapted for quantification of arterial flow [33]. While it appears that an assumption of Poiseuille flow (fully developed parabolic profile) could be used to estimate WSS at the time of peak flow (figure 5*b*(i)), it is evident that a parabolic fit does not accurately capture near-wall velocity at the time of minimum flow (figure 5*b*(ii)). The WSS experienced by the endothelium was calculated from the PIV measurements at a resolution comparable with the size of a single cell (14.6 μm).

Four ROIs downstream of stent struts were examined and compared with an ROI far enough downstream of the stent (2 mm) to be representative of the undisturbed flow field (figure 5*a*). The time-varying WSS within each ROI was estimated from the near-wall velocity field (figure 5*c*). The WSS profiles in all ROIs (figure 5*d*(i)) were qualitatively similar to the centreline flow velocity profile (figure 5*d*(ii)) as well as the driving pressure wave in the *in vitro* artery (figure 1*d*). The mean time-averaged WSS in all stent ROIs was significantly lower than the mean WSS in the downstream ROI ($p \leq 0.0001$) except stent ROI 3 ($p = 0.6341$), and all stent ROIs had significantly different mean WSS from one another ($p < 0.0001$) except ROI 1 versus ROI 4 ($p = 0.9537$) (figure 5*e*).

The numerical simulation reveals WSS profiles and values similar to the experimental data (figure 6). The time-varying WSS is nearly synchronized with the centreline velocity and follows a similar profile (figure 6*c*). The time-averaged WSS is lower within the stented region than in the downstream ROI (figure 6*d*). The primary difference between the results of experiment and simulation is in the magnitude of WSS. The downstream time-averaged WSS in the simulated *in vitro* artery is identical to that predicted by theory, while the WSS measured experimentally using PIV is less than a third of that value, most probably due to vessel curvature, flow asymmetry and the presence of three-dimensional flow patterns.

4. Discussion

The *in vitro* artery provides a versatile platform for quantitative dynamic studies of cellular behaviour in a configuration mimicking blood vessels. In this paper, we have studied the response of ECs and SMCs to the implantation of a stent in an *in vitro* artery designed to mimic a coronary artery. The results obtained are coherent with observations *in vivo*, as discussed below, and demonstrate the potential of this novel platform for future work in cardiovascular research.

The state of the endothelium in the *in vitro* artery before, during, and after stent implantation was carefully studied. Interestingly, large patches of endothelium as well as scattered cells remained viable within the stent immediately after stent deployment. This observation is consistent with the findings of a recent study that compared *in vivo* histology with

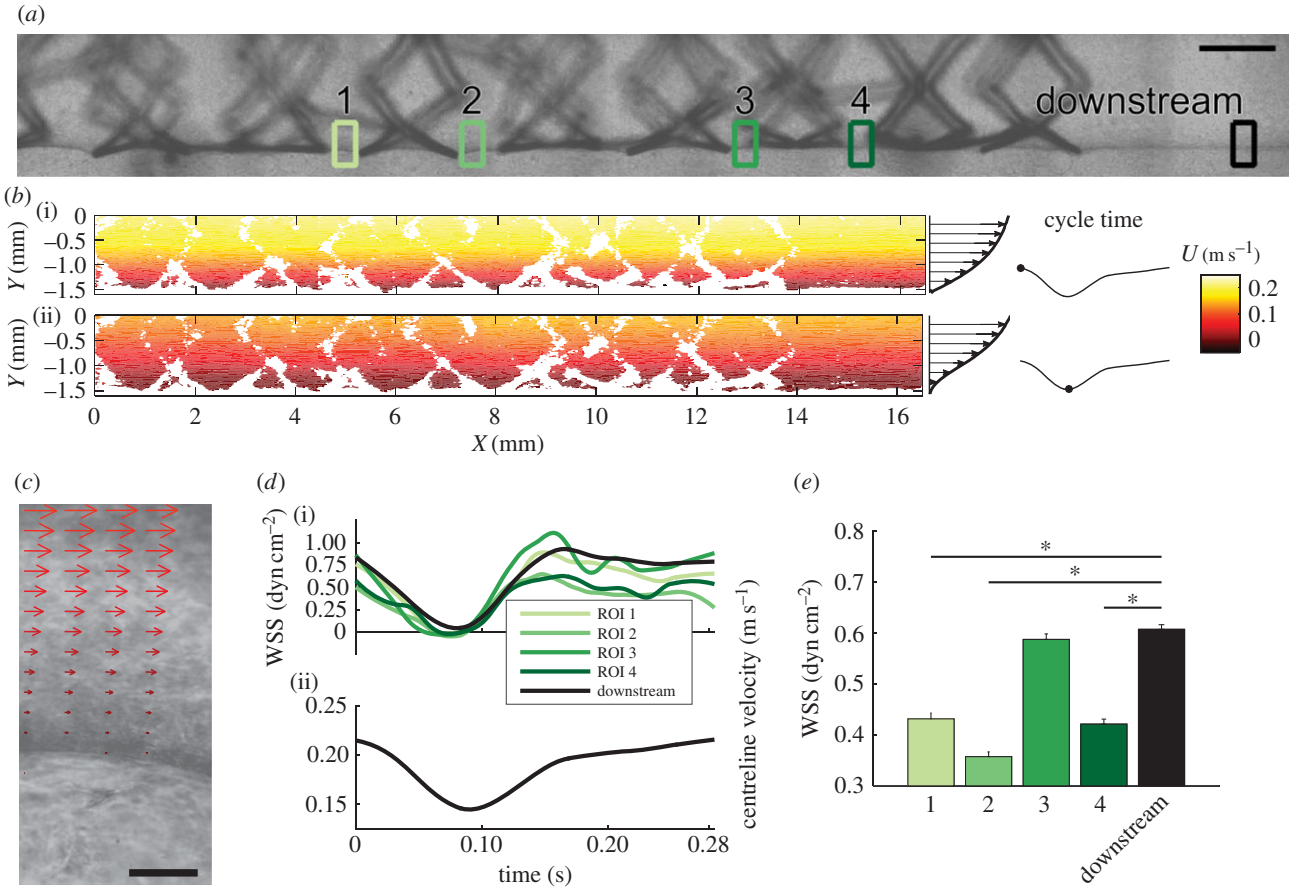

Figure 5. Flow in the stentable *in vitro* artery. (*a*) Phase-contrast image indicating regions of interest (ROIs) in which wall shear stress (WSS) was calculated. Four regions immediately downstream of stent struts were investigated and compared with a control region far downstream of the stent. Scale bar, 1 mm. (*b*) Velocity fields and longitudinally averaged velocity profiles obtained using particle image velocimetry and used for quantification of WSS at two different time points during the pulsatile cycle. While the flow appears parabolic at the time of peak flow (i), the velocity field at minimum flow (ii) reveals irregularities around stent struts with reversal at the wall. (*c*) Sample vector field for ROI 1 at the time of peak mean flow. Scale bar, 100 μm. The vectors are coloured according to the colourmap in (*b*). For clarity, only 1 in 4 vectors is shown. (*d*) The WSS within each ROI (i) follows a similar profile to the centreline velocity in the channel (ii). The WSS is smoothed (for visualization only) using a rloess filter. (*e*) Small yet significant differences are present between the mean WSS of ROIs 1, 2 and 4 and the downstream WSS. $^*p < 0.0001$. Error bars represent s.e.m.

computational models of re-endothelialization in order to understand mechanisms of endothelial repair after stenting [34]. Tahir *et al*. performed computations contrasting the scenarios of random seeding of ECs within the stent with the case permitting EC growth from only outside the stented section and found that the random seeding model was more consistent with *in vivo* endothelial growth patterns. Based on this study, it appears that EC viability patterns within the stented portion of our *in vitro* artery succeed in mimicking important aspects of *in vivo* conditions.

The *in vitro* artery was designed to achieve flow similarity with human coronary flow by matching Reynolds and Womersley numbers because these two dimensionless parameters determine the structure of the flow field within the vessel and its evolution over the pulsatile cycle. The design also includes a constraint of non-scalable geometry, as endovascular devices are not scalable. A notable consequence of matching Reynolds and Womersley numbers for flow similarity is that the WSS within the *in vitro* artery is not matched to that present in the coronary artery *in vivo*. More specifically, for Poiseuille flow in a cylindrical vessel, $\mathrm{WSS} = 4\mu Q/\pi R^3$, where μ is the dynamic viscosity, Q is the volumetric flow rate, and R is the vessel radius. The Reynolds number in a cylindrical vessel is $Re = 2\rho Q/\pi R$, where ρ is the fluid density. Therefore, Reynolds number and vessel diameter matching between the *in vitro* artery and *in vivo* conditions leads to the WSS in the *in vitro* artery scaling by the square of the ratio of the viscosities of blood and cell culture medium.

As the viscosity of the culture media used in this study was 0.78 mPa s while the viscosity of blood is 3.5 mPa s [35], the WSS in the *in vitro* artery is expected to be approximately 20 times lower than *in vivo*. Accordingly, the PIV-measured mean downstream WSS of 0.06 Pa (0.6 dyn cm^{-2}) in the *in vitro* artery scales to approximately 1.2 Pa (12 dyn cm^{-2}) using blood viscosity, which is a close match with *in vivo* measurements of 0.33–1.24 Pa (3.3–12.4 dyn cm^{-2}) in the human coronary artery as reported by Doriot *et al*. [35]. Because *in vivo* WSS varies strongly spatially within arteries due to vessel curvature [36] and *in vivo* WSS measurements are subject to significant uncertainty themselves due to the low resolution of velocity measurements and assumptions of Poiseuille flow [35,37], this agreement between *in vivo* and *in vitro* data is more than satisfactory. Furthermore, the numerical simulation reproduces the flow and WSS patterns obtained experimentally even under the idealized conditions assumed for the CFD computations.

The presence of reduced WSS in regions between stent struts in the *in vitro* artery (obtained both experimentally and numerically) is consistent with the conclusions of Charonko *et al*., who measured WSS around stent struts in a silicone

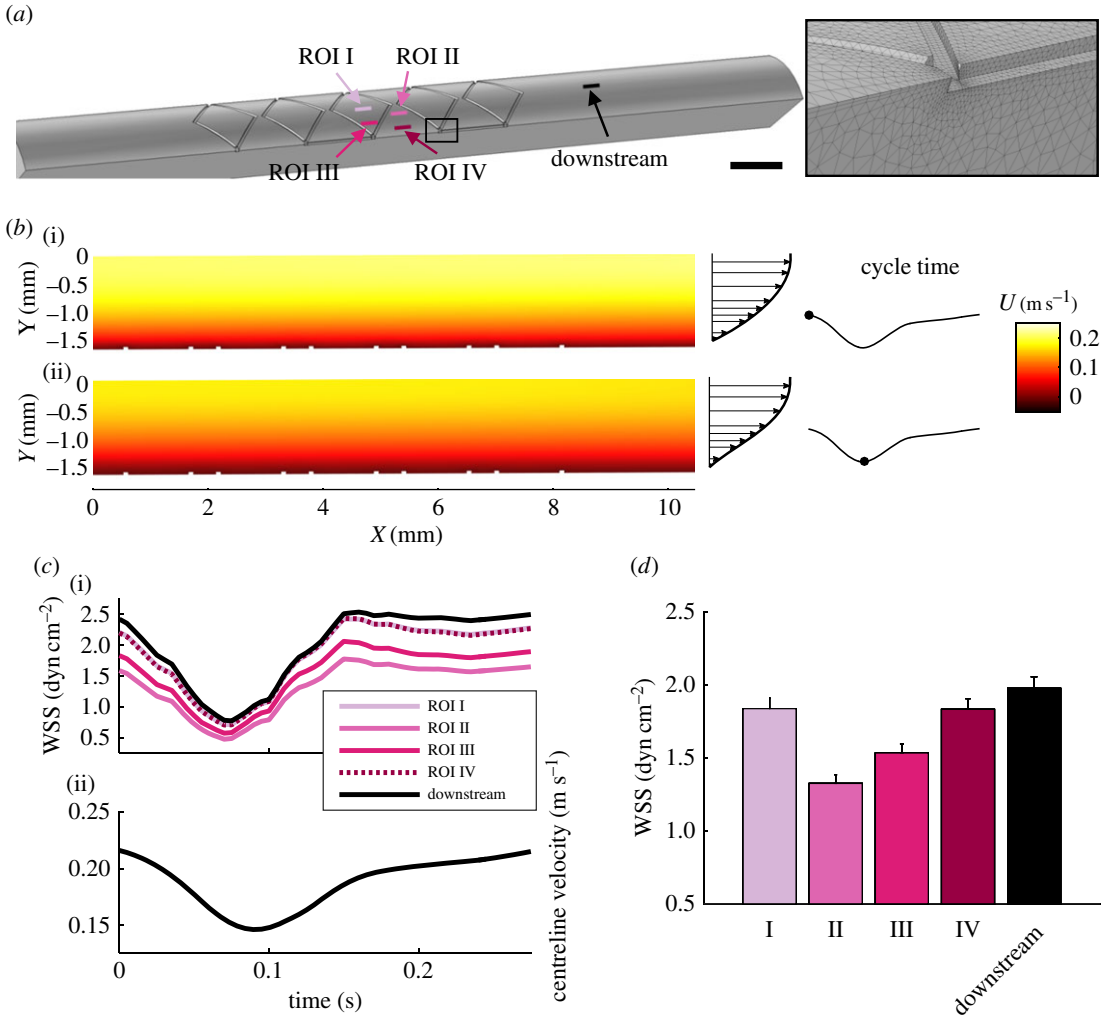

Figure 6. Computational model of the flow field in the stentable *in vitro* artery. (*a*) Model geometry indicating regions of interest (ROIs) in which wall shear stress (WSS) was calculated. Except for the downstream ROI, these ROIs do not correspond to the ROIs in figure 5. Scale bar, 1 mm. Inset: sample of mesh used for computation. (*b*) Velocity fields and longitudinally averaged velocity profiles resulting from the numerical simulation. As in the experimental results (figure 5*b*), the velocity profile is clearly not parabolic at the time of minimum flow. (*c*) The WSS in the simulation ROIs follows a similar pattern to the experimental data, with all ROIs within the stent presenting lower WSS throughout the cycle than the downstream ROI. Here, the greatest deviations from the downstream WSS occur for ROIs closest to stent struts. The WSS profiles for ROI I and ROI IV overlap nearly identically despite the difference in position. (*d*) The time-averaged WSS in the simulated *in vitro* artery is lower near and between stent struts than in the downstream region, validating the experimental measurements.

tube [29], and Seo *et al*., who simulated arterial flow around stent struts in an idealized geometry [38]. Although the overall differences in measured time-averaged WSS among the different ROIs are small (figure 5*e*) the time-dependent WSS results demonstrate that these differences are considerably larger during the period of flow acceleration than during deceleration and that variations in WSS temporal gradients are even more pronounced (figure 5*d*). Such variation could contribute to significant alterations in endothelial behaviour, as ECs are thought to respond to both time-averaged WSS as well as temporal gradients in WSS [39]. Finally, the mean WSS measured within each ROI is three to five times lower than the WSS estimated by assuming ideal flow conditions (Poiseuille flow) or from numerical simulation. The Poiseuille flow estimate of WSS assumes axisymmetric flow; however, under the flow conditions in the *in vitro* artery this axisymmetric mode is likely unstable [40]. This result demonstrates the importance of measurement of WSS rather than estimation based on idealized analytical or numerical models.

The stentable *in vitro* artery certainly is not without its limitations. Owing to the design objective of transparency for brightfield and fluorescence imaging, the seeding density of SMCs in the hydrogel is far lower than *in vivo*. Therefore, interactions between SMCs and ECs and biochemical cues are likely to be reduced in magnitude and perhaps complexity. Additionally, the rigid FEP housing of the *in vitro* artery (necessary for imaging while maintaining an axisymmetric hydrogel) inhibits changes in lumen diameter as occurs during vasodilation or vasoconstriction. There are other limitations that can and will be addressed in future work. Currently, inflammatory and other biological factors found in blood are absent from the perfusion media. This deficiency may explain the accelerated endothelial healing rate in the *in vitro* artery compared with *in vivo* data. Conversely, the sub-physiological temperature within the *in vitro* artery likely has an inhibitory effect on the endothelial migration rate while increasing cellular proliferation [41,42]. Future studies will introduce biological factors and temperature variation and examine their effects on cellular response to endothelial wounding. Indeed, an advantage of the *in vitro* artery is that such factors can be individually controlled in order to provide a more mechanistic understanding of their role in regulating EC and SMC responses. The effect of the reduction in WSS in the *in vitro* artery caused by viscosity mismatch between cell culture

medium and blood is unknown but may be important for endothelial response. In future studies, the viscosity of the cell culture medium can be increased to match the viscosity of blood through the addition of thickening, although it would be important to first establish that such agents have a minimal effect on endothelial and SMC function. Finally, the current design of the *in vitro* artery incorporates a single layer of hydrogel containing SMCs. However, the system can be easily adapted for bi- or tri-layer configurations and additional cell types such as fibroblasts, as was done by Hasan *et al*. [14]. Despite these limitations, the *in vitro* artery can already serve as a robust platform for comparative research for applications such as informed design of stent geometry or drug release profiles.

We believe that the *in vitro* artery provides a model system within which the biological performance of endovascular devices can be tested prior to proceeding to animal trials. Indeed, we hope that a key additional benefit of this system will be to reduce the use of animals in vascular research. The short time scale of endothelial wound healing post-stenting—of the order of one day—contributes to the utility of the *in vitro* artery for such research. By virtue of its integration of an advanced *in vitro* tissue platform with automated data processing modules for quantification of cell behaviour and flow parameters, the *in vitro* artery described here is not only ideal for device assessment and optimization but can also be adapted for use in a host of vascular investigations including toxicity testing of cardiovascular drugs, dynamic monitoring of leukocyte interaction with the arterial wall during inflammation and assessment of the effects of nanomaterials on the arterial wall.

Authors' contributions. E.E.A. designed and carried out experiments, analysed the data and wrote the manuscript. F.P.C. performed numerical simulations, analysed the data and wrote the manuscript. A.I.B. conceived of the study, analysed the data and wrote the manuscript. All authors gave final approval for publication.

Competing interests. We declare we have no competing interests.

Funding. E.E.A. was funded by a Whitaker International Program post-doctoral fellowship. F.P.C. was funded by a doctoral fellowship from the Ecole Normale Supérieure. This work was supported in part by an endowment in Cardiovascular Cellular Engineering from the AXA Research Fund.

Acknowledgement. The authors thank Prof Antoine Lafont for providing the stents used in this study.

References

1. Hartung T, Daston G. 2009 Are *in vitro* tests suitable for regulatory use? *Toxicol. Sci*. **111**, 233–237. (doi:10.1093/toxsci/kfp149)
2. Rogers C, Tseng DY, Squire JC, Edelman ER. 1999 Balloon-artery interactions during stent placement? a finite element analysis approach to pressure, compliance, and stent design as contributors to vascular injury. *Circ. Res*. **84**, 378–383. (doi:10.1161/01.RES.84.4.378)
3. Iqbal J, Gunn J, Serruys PW. 2013 Coronary stents: historical development, current status and future directions. *Br. Med. Bull*. **106**, 193–211. (doi:10.1093/bmb/ldt009)
4. Fisher AB, Chien S, Barakat AI, Nerem RM. 2001 Endothelial cellular response to altered shear stress. *Am. J. Physiol. Lung Cell. Mol. Physiol*. **281**, L529–L533.
5. Campbell JH, Campbell GR. 2012 Smooth muscle phenotypic modulation—a personal experience. *Arterioscler. Thromb. Vasc. Biol*. **32**, 1784–1789. (doi:10.1161/ATVBAHA.111.243212)
6. Balcells M, Martorell J, Olivé C, Santacana M, Chitalia V, Cardoso AA, Edelman ER. 2010 Smooth muscle cells orchestrate the endothelial cell response to flow and injury. *Circulation* **121**, 2192–2199. (doi:10.1161/CIRCULATIONAHA.109.877282)
7. Ziegler T, Alexander RW, Nerem RM. 1995 An endothelial cell-smooth muscle cell co-culture model for use in the investigation of flow effects on vascular biology. *Ann. Biomed. Eng*. **23**, 216–225. (doi:10.1007/BF02584424)
8. Truskey GA. 2011 Endothelial cell vascular smooth muscle co-culture assay for high throughput screening assays. *Int. J. High Throughput Screen*. **2010**, 171–181. (doi:10.2147/IJHTS.S13459)
9. Antoine EE, Vlachos PP, Rylander MN. 2014 Review of collagen I hydrogels for bioengineered tissue microenvironments: characterization of mechanics, structure, and transport. *Tissue Eng. B Rev*. **20**, 1–14. (doi:10.1089/ten.TEB.2014.0086)
10. Liu J, Zheng H, Poh P, Machens H-G, Schilling A. 2015 Hydrogels for engineering of perfusable vascular networks. *Int. J. Mol. Sci*. **16**, 15 997–16 016. (doi:10.3390/ijms160715997)
11. Yamagishi Y, Masuda T, Matsusaki M, Akashi M, Yokoyama U, Arai F. 2014 Microfluidic perfusion culture system for multilayer artery tissue models. *Biomicrofluidics* **8**, 064113. (doi:10.1063/1.4903210)
12. Jung Y, Ji H, Chen Z, Fai Chan H, Atchison L, Klitzman B, Truskey G, Leong KW. 2015 Scaffold-free, human mesenchymal stem cell-based tissue engineered blood vessels. *Sci. Rep*. **5**, 15116. (doi:10.1038/srep15116)
13. Fernandez CE, Yen RW, Perez SM, Bedell HW, Povsic TJ, Reichert WM, Truskey GA. 2016 Human vascular microphysiological system for *in vitro* drug screening. *Sci. Rep*. **6**, 21579. (doi:10.1038/srep21579)
14. Hasan A, Paul A, Memic A, Khademhosseini A. 2015 A multilayered microfluidic blood vessel-like structure. *Biomed. Microdevices* **17**, 9993. (doi:10.1007/s10544-015-9993-2)
15. Bhatia SN, Ingber DE. 2014 Microfluidic organs-on-chips. *Nat. Biotechnol*. **32**, 760–772. (doi:10.1038/nbt.2989)
16. Benam KH *et al*. 2015 Engineered *in vitro* disease models. *Annu. Rev. Pathol*. **10**, 195–262. (doi:10.1146/annurev-pathol-012414-040418)
17. Antoine EE, Vlachos PP, Rylander MN. 2015 Tunable collagen I hydrogels for engineered physiological tissue micro-environments. *PLoS ONE* **10**, e0122500. (doi:10.1371/journal.pone.0122500)
18. Buchanan CF, Voigt EE, Szot CS, Freeman JW, Vlachos PP, Rylander MN. 2014 Three-dimensional microfluidic collagen hydrogels for investigating flow-mediated tumor-endothelial signaling and vascular organization. *Tissue Eng. C Methods* **20**, 64–75. (doi:10.1089/ten.tec.2012.0731)
19. Hinderliter PM, Minard KR, Orr G, Chrisler WB, Thrall BD, Pounds JG, Teeguarden JG. 2010 ISDD: a computational model of particle sedimentation, diffusion and target cell dosimetry for *in vitro* toxicity studies. *Part. Fibre Toxicol*. **7**, 36. (doi:10.1186/1743-8977-7-36)
20. Edelstein A, Amodaj N, Hoover K, Vale R, Stuurman N. 2010 Computer control of microscopes using μManager. *Curr. Protoc. Mol. Biol*. **92**, 14.20.1–14.20.17. (doi:10.1002/0471142727.mb1420s92)
21. Schindelin J *et al*. 2012 Fiji: an open-source platform for biological-image analysis. *Nat. Methods* **9**, 676–682. (doi:10.1038/nmeth.2019)
22. Meinhart CD, Wereley ST, Santiago JG. 1999 PIV measurements of a microchannel flow. *Exp. Fluids* **27**, 414–419. (doi:10.1007/s003480050366)
23. Olsen MG, Adrian RJ. 2000 Out-of-focus effects on particle image visibility and correlation in microscopic particle image velocimetry. *Exp. Fluids* **29**, S166–S174. (doi:10.1007/s003480070018)
24. Poelma C, Vennemann P, Lindken R, Westerweel J. 2008 *In vivo* blood flow and wall shear stress measurements in the vitelline network. *Exp. Fluids* **45**, 703–713. (doi:10.1007/s00348-008-0476-6)
25. Eckstein A, Vlachos PP. 2009 Assessment of advanced windowing techniques for digital particle image velocimetry (DPIV). *Meas. Sci. Technol*. **20**, 075402. (doi:10.1088/0957-0233/20/7/075402)
26. Eckstein A, Vlachos PP. 2009 Digital particle image velocimetry (DPIV) robust phase correlation. *Meas.*

Sci. Technol. **20**, 055401. (doi:10.1088/0957-0233/20/5/055401)

27. Meinhart CD, Wereley ST, Santiago JG. 2000 A PIV algorithm for estimating time-averaged velocity fields. *J. Fluids Eng*. **122**, 285–289. (doi:10.1115/1.483256)
28. Westerweel J, Scarano F. 2005 Universal outlier detection for PIV data. *Exp. Fluids* **39**, 1096–1100. (doi:10.1007/s00348-005-0016-6)
29. Charonko J, Karri S, Schmieg J, Prabhu S, Vlachos P. 2009 *In vitro*, time-resolved PIV comparison of the effect of stent design on wall shear stress. *Ann. Biomed. Eng*. **37**, 1310–1321. (doi:10.1007/s10439-009-9697-y)
30. Karri S, Charonko J, Vlachos PP. 2009 Robust wall gradient estimation using radial basis functions and proper orthogonal decomposition (POD) for particle image velocimetry (PIV) measured fields. *Meas. Sci. Technol*. **20**, 045401. (doi:10.1088/0957-0233/20/4/045401)
31. Humphrey JD. 2002 *Cardiovascular solid mechanics: cells, tissues, and organs*. Berlin, Germany: Springer Science & Business Media.
32. KolandaiveluK, Leiden BB, Edelman ER. 2014 Predicting response to endovascular therapies: dissecting the roles of local lesion complexity, systemic comorbidity, and clinical uncertainty. *J. Biomech*. **47**, 908–921. (doi:10.1016/j.jbiomech.2014.01.006)
33. Vennemann P, Lindken R, Westerweel J. 2007 *In vivo* whole-field blood velocity measurement techniques. *Exp. Fluids* **42**, 495–511. (doi:10.1007/s00348-007-0276-4)
34. Tahir H, Bona-Casas C, Narracott AJ, Iqbal J, Gunn J, Lawford P, Hoekstra AG. 2014 Endothelial repair process and its relevance to longitudinal neointimal tissue patterns: comparing histology with in silico modelling. *J. R. Soc. Interface* **11**, 20140022. (doi:10.1098/rsif.2014.0022)
35. Doriot PA, Dorsaz PA, Dorsaz L, De Benedetti E, Chatelain P, Delafontaine P. 2000 In-vivo measurements of wall shear stress in human coronary arteries. *Coron. Artery Dis*. **11**, 495–502. (doi:10.1097/00019501-200009000-00008)
36. Asakura T, Karino T. 1990 Flow patterns and spatial distribution of atherosclerotic lesions in human coronary arteries. *Circ. Res*. **66**, 1045–1066. (doi:10.1161/01.RES.66.4.1045)
37. Reneman RS, Hoeks APG. 2008 Wall shear stress as measured *in vivo*: consequences for the design of the arterial system. *Med. Biol. Eng. Comput*. **46**, 499–507. (doi:10.1007/s11517-008-0330-2)
38. Seo T, Schachter LG, Barakat, AI. 2005 Computational study of fluid mechanical disturbance induced by endovascular stents. *Ann. Biomed. Eng*. **33**, 444–456. (doi:10.1007/s10439-005-2499-y)
39. White CR, Stevens HY, Haidekker M, Frangos JA. 2005 Temporal gradients in shear, but not spatial gradients, stimulate ERK1/2 activation in human endothelial cells. *Am. J. Physiol. Heart Circ. Physiol*. **289**, H2350–H2355. (doi:10.1161/01.CIR.103.20.2508)
40. Voigt EE, Buchanan CF, Rylander MN, Vlachos PP. 2012 Wall shear stress measurements in an arterial flow bioreactor. *Cardiovasc. Eng. Technol*. **3**, 101–111. (doi:10.1007/s13239-011-0076-0)
41. Yang QR, Vanden Berghe D. 1995 Effect of temperature on *in vitro* proliferative activity of human umbilical vein endothelial cells. *Experientia* **51**, 126–132. (doi:10.1007/BF01929355)
42. Osada T, Iijima K, Tanaka H, Hirose M, Yamamoto J, Watanabe S. 1999 Effect of temperature and mechanical strain on gastric epithelial cell line GSM06 wound restoration *in vitro*. *J. Gastroenterol. Hepatol*. **14**, 489–494. (doi:10.1046/j.1440-1746.1999.01890.x)